

# The Model of Decomposition of a Fe–Cu Alloy with Concentration-Depending Interatomic Interactions

I. K. Razumov<sup>a,\*</sup> and I. G. Shmakov<sup>a</sup>

<sup>a</sup> *Mikheev Institute of Metal Physics, Ural Branch, Russian Academy of Science, Yekaterinburg, Russia*

\**e-mail: rik@imp.uran.ru*

Received January 21, 2019; revised January 21, 2019; accepted January 22, 2019

**Abstract**—The thermodynamics and kinetics of decomposition of a Fe–Cu alloy are investigated in the context of a simple ab initio parameterization model taking into account the concentration dependence of the magnetic contribution to the free energy. It is shown that taking into account a difference between the short-range and long-range magnetic orders near the Curie temperature is very important for calculating the solubility of copper in iron. The solubility of copper in bcc iron and the stability limit of a homogeneous state (physical spinodal) are evaluated via the kinetic Monte Carlo method. The impact of structural defects (dislocations and grain boundaries) on these curves, as well as on the kinetic time–temperature–transformation (TTT) diagram, is also discussed.

DOI: 10.1134/S1063783419060180

## 1. INTRODUCTION

In the last years, there is a high interest in using copper as a doping element in the fabrication of steel [1–3] due to the reinforcing effect of bcc-Cu nano-precipitates coherent with a matrix which appear at the cooling of a solid solution [4]. When those enrich ~10 nm in size, their coherence with iron matrix vanishes and the lattice transforms into an fcc crystal structure, leading to embrittlement of the material [5, 6]. Thus, the kinetics of initial stages of decomposition, as well as mechanisms of possible stabilization of bcc-Cu nano-precipitates is of particular attention. Studying this challenge necessitates a sequential model that takes into account the concentration dependence of interatomic interactions and the role of magnetism in the development of phase transformation [7–9].

Indeed, the deviation of solubility of copper in iron from the Arrhenius law, observed within a broad range above and below the Curie point,  $T_C$ , cannot be explained in the context of classical models (such as the model of regular solid solution [10]) [11–13]. The essential role of magnetism in the decomposition of iron alloys was emphasized by Zener [14, 15]. Meanwhile, before now, the change in the magnetic energy upon the decomposition of the Fe–Cu alloy was neglected [16–18], or there was used a quite simplified Cu–Cu interaction potential depending on only the temperature [7] at accounting no difference between the solubility and stability limits of the homogeneous state [19]. The authors of work [20] used the tempera-

ture-depending interatomic interaction parameters that were found via the fitting to experimental data.

Since the magnetism exists in only the iron matrix, but it is absent in the bulk of copper precipitates, the consistent theory of decomposition of the Fe–Cu alloy is expected to take into account the concentration dependence of interatomic interactions. The mixture potentials  $W_{\text{mix}}$  in the para- and ferromagnetic states of iron were calculated as a function of concentration via EMT0-CPA (exact muffin-tin orbitals, coherent potential approximation) [7] and MCE (magnetic cluster expansion) [21] approaches. These results can be fundamental for constructing the theory of decomposition of the Fe–Cu alloy based on the ab initio parametrization.

Work [9] reports the effective concentration-depended Cu–Cu interaction potential, which accounts for the role of magnetism via the ab initio calculations [7], as well as the theoretical solubility limit was calculated in accordance with experimental data. In this respect, the present study aims to further development of the approach proposed. Particular attention will be paid to the thermodynamics and kinetics of transformations in the vicinity of the Curie temperature. In particular, the key importance to take into account the difference between the long-range and short-range magnetic orders will be discussed, the nonmonotonic temperature behavior of the physical spinodal will be established, and the effect of structural defects on the physical spinodal and the time–temperature–transformation (TTT) diagram will be elucidated, as well. This will enable one to thoroughly

describe the thermodynamic and kinetic features of decomposition in a diluted Fe–Cu alloy, using the concentration and temperature dependences of inter-atomic interactions.

## 2. THE FREE ENERGY OF THE Fe–Cu ALLOY WITH A CONCENTRATION DEPENDENT MAGNETIC CONTRIBUTION

Let us consider the configuration Hamiltonian containing the paramagnetic (PM) state contribution,  $H_{\text{PM}}$ , as a series of  $n_i$  [22], and the spin interaction energy  $H_{\text{mag}}$  in the Heisenberg form:

$$H = H_{\text{PM}} + H_{\text{mag}},$$

$$H_{\text{PM}} = E_0 + \varepsilon \sum_i n_i + \frac{1}{2} \sum_{i,j} V_{ij}^{\text{PM}} n_i n_j + \dots, \quad (1)$$

$$H_{\text{mag}} = \frac{1}{2} \sum_{i,j} Y_{ij} \sigma_i \sigma_j (1 - n_i)(1 - n_j),$$

where  $n_i$  are the node occupation numbers (being 1, if the Cu atom is found in the  $i$ th node 1, otherwise 0);  $\sigma_i$  is a spin value on the  $i$ th node (a spin is assumed to be normalized with reference to 1);  $Y_{ij}$  is a spin exchange interaction parameter;  $\varepsilon$  is the change in the energy of a system, caused by the introduction of a singular Cu atom; and  $V_{ij}^{\text{PM}}$  is a potential of the Cu–Cu interaction in the PM-state. In order to consider the multiparticle interactions in the expression for  $H_{\text{PM}}$ , let us limit ourselves to the effective pair potential depending on the local Cu concentration, i.e.,  $V_{ij}^{\text{PM}} = V_{ij}^{\text{PM}}(c_i)$ , where  $c_i = \langle n_i \rangle$  is the Cu concentration on the  $i$ th node in the mean field approximation.

Subject Eq. (1) to the averaging over the atomic and spin configurations, assuming only the nearest spins interact and a slight variation in the concentration  $c_i$  at the distances around of the lattice parameter. After that, let us pass to the continual representation of the internal energy density of the alloy (by neglecting linear contributions), as follows:

$$g(c) = v_{\text{PM}}(c)c^2 - J(c)Q_1(c)(1 - c)^2, \quad (2)$$

where  $Q_1 = Q(|r_i - r_j|) = \langle \sigma_i \sigma_j \rangle$  is a nearest-neighbor spin correlator,  $J(c) = \frac{1}{2} \sum_j Y_{ij}(c_i)$ ,  $v_{\text{PM}}(c) = \frac{1}{2} \sum_j V_{ij}^{\text{PM}}(c_i)$ . The mixing potentials  $W_{\text{mix}}(c) = E_{\text{mix}}(c)/[c(1 - c)]$  in the para- and ferromagnetic states were calculated via the EMT0-CPA [7] and MCE approach [21]; herewith, the mixing energy is  $E_{\text{mix}}(c) = g(c) - (1 - c)E_{\text{Fe}} - cE_{\text{Cu}}$ , where  $E_{\text{Fe}}$ ,  $E_{\text{Cu}}$  are the energies of pure bcc Fe and Cu. In the above designations,  $E_{\text{Fe}} = g(c = 0) = -J_0 Q_1^0$ ,  $Q_1^0 = Q_1(c = 0)$ ,

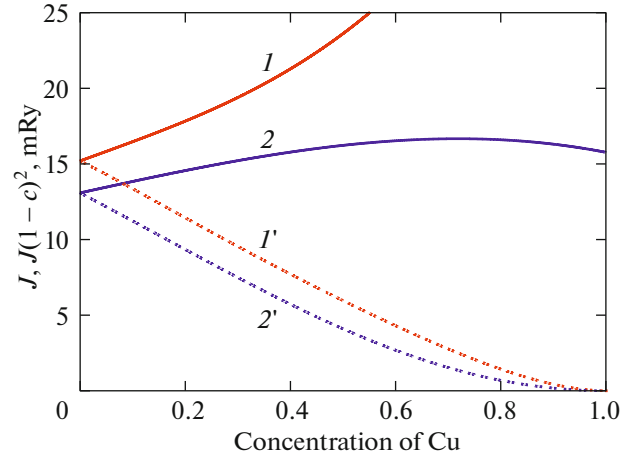


Fig. 1. Exchange energy  $J(c)$  as a function of copper concentration in accordance with (1) EMT0-CPA and (2) MCE calculations; the corresponding product  $J(c)(1 - c)^2$  ( $1'$ ,  $2'$ ).

$E_{\text{Cu}} = g(c = 1) = v_{\text{PM}}(1)$ . Accounting for  $Q_1^{\text{PM}} = 0$ ,  $Q_1^{\text{FM}} = 1$ , Eq. (2) yields in the equation below:

$$J(c) = \frac{J(0) - (W_{\text{mix}}^{\text{FM}}(c) - W_{\text{mix}}^{\text{PM}}(c))c}{(1 - c)}. \quad (3)$$

Using the representation  $J(c) = J_0 + J_1 c + J_2 c^2 + J_3 c^3$ , the coefficients in accordance with EMT0-PCA are:  $J_0 = 15.2$ ,  $J_1 = 12.7$ ,  $J_2 = -1.6$ ,  $J_3 = 20$  (mRy) and those provided by MCE are:  $J_0 = 13.086$ ,  $J_1 = 7.698$ ,  $J_2 = -0.528$ ,  $J_3 = -4.523$  (mRy). In both cases, the  $J$  value increases with Cu concentration (see Fig. 1); however, the MCE results seem to be more adequate at large concentrations. It is worth mentioning that the product  $J(c)(1 - c)^2$ , defining the magnetic contribution in the energy (2), is found to be at least comparable for the two methods (see curves  $1'$  and  $2'$ ).

The energy  $v_{\text{PM}}(c)$  in Eq. (2) is evaluated from ab initio  $W_{\text{mix}}^{\text{PM}}(c)$  data. Remembering that  $Q_1^{\text{PM}} = 0$  and substituting Eq. (2) in the definition of  $E_{\text{mix}}(c)$ , one obtains

$$W_{\text{mix}}^{\text{PM}}(c) = \frac{-v_{\text{PM}}(1) + v_{\text{PM}}(c)c}{1 - c}. \quad (4)$$

It is easy to see from data [7] that the  $v_{\text{PM}}(c)$  dependence is weak that allows one to assume  $v_{\text{PM}}(c) = -28.8$  mRy = const.

The local Curie temperature  $T_C(c)$  can be established from the relationship below:

$$T_C(c) = T_C(0)(1 - c)J(c)/J(0) \quad (5)$$

which is valid in both the Curie–Weiss theory, as well as the more accurate quasi-chemical approximation and cluster methods [23]. Note that the Curie tem-

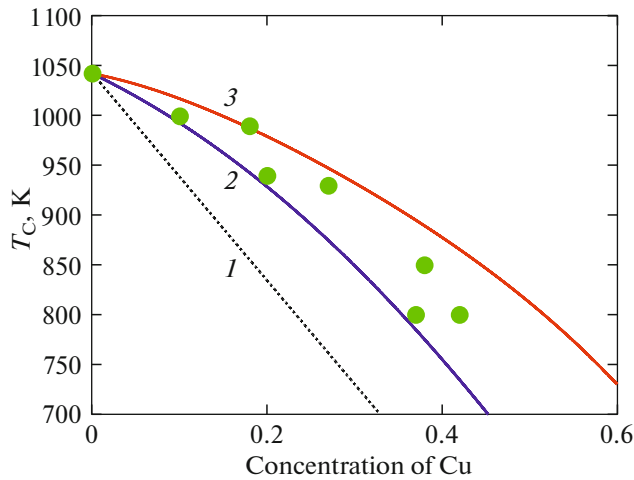


**Fig. 2.** Curie temperature as a function of copper concentration (1) in assuming  $J(c) = \text{const}$ , as well as based from (2) MCE and (3) EMTO-CPA calculation models. The circles correspond to experimental data [24].

perature in pure  $\alpha$ -Fe is  $T_C(0) = 1043$  K. Figure 2 displays the  $T_C(c)$  plots obtained in assuming that  $J(c) = J(0) = \text{const}$  (curve 1), as well as the  $J(c)$  derived from MCE (curve 2) and EMTO-CPA (curve 3) methods. As seen, an increase in  $J(c)$  with copper concentration leads to a convex  $T_C(c)$  profile in accordance with experimental results [24].

Figure 3 shows various variants of the nearest-neighbor spin correlator for pure  $\alpha$ Fe: the long-range magnetic order  $Q_1(T) = m^2(T/T_C)$  only and the application of the empirical equation of magnetization [25] (curve 1); the short-range magnetic order at  $T > T_C$  in the qualitative coincidence with the Oguchi theory [26] (curve 2); the same correlator after smoothing (curve 3), and the correlator proposed in the model with a spin–lattice dynamics [27] (curve 4). Note that the correlator is a function of copper concentration because of the  $T_C(c)$  dependence (Eq. (5)). The formulas for constructing the correlators are available in Appendix A. As seen in Fig. 3, at  $T < T_C$  the correlator of the model [27] reduces considerably the degree of magnetic order in comparison with the empirical curve [25]. Thus, a smoothed correlator based on the empirical  $m(T)$  function with a short-range order at  $T > T_C$  (curve 3) is further considered as preferable.

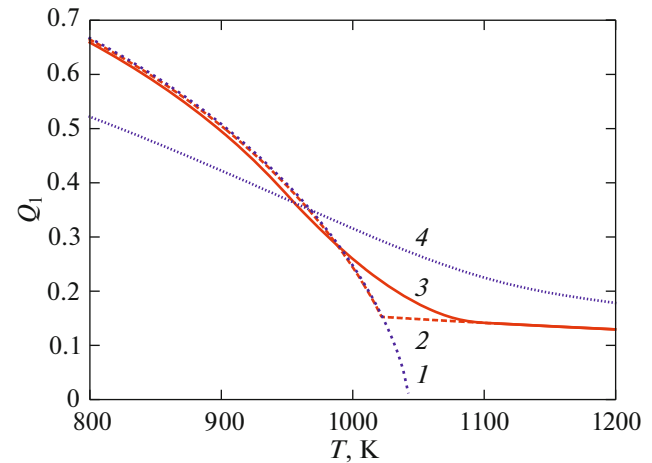
The free energy density is expressed as

$$f(c) = g(c) - TS, \quad (6)$$

where the configuration entropy  $S$  is defined in the approximation of regular solid solution [10]:

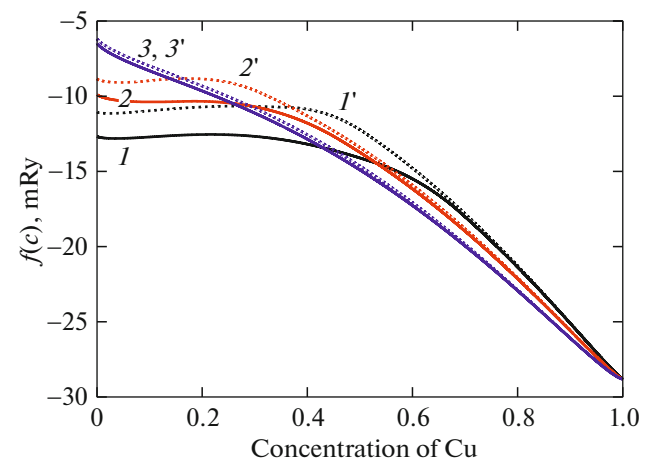
$$S = -k[c \ln c + (1 - c) \ln(1 - c)]. \quad (7)$$

Figure 4 displays the  $f(c)$  dependence plotted at different temperatures using a correlator with the short-range magnetic order at  $T > T_C$  (curve 3 in Fig. 3). The



**Fig. 3.** Nearest-neighbor spin correlator in pure  $\alpha$ -Fe (1) from the empirical equation for magnetization [25], (2) including the short-range order at  $T > T_C$ , (3) after smoothing, (4) according to the spin-lattice dynamics model [27].

main feature of the  $f(c)$  plot is a characteristic plateau at low copper concentrations ( $c < 0.4$ ), caused by the magnetic contribution to the energy. Starting from the homogeneous state, the decomposition tendency is weak or missing within the plateau range; i.e., a homogeneous alloy remains stable relative to infinitely small composition fluctuations in concave segments of the  $f(c)$  curve [10]. This means that insignificant addition contributions to the energy may lead to the emergence of local free energy minima in a plateau range. This seems to provoke the formation of precipitates of intermediate composition phases observed in FeCu-based hard alloys [28].



**Fig. 4.** Free energy density of alloy as a function of copper concentration at  $T = 700$  K (1, 1'), 900 K (2, 2'), 1100 K (3, 3'), with parametrization  $J(c)$  based on (1–3) EMTO-CPA and (1'–3') MCE models.

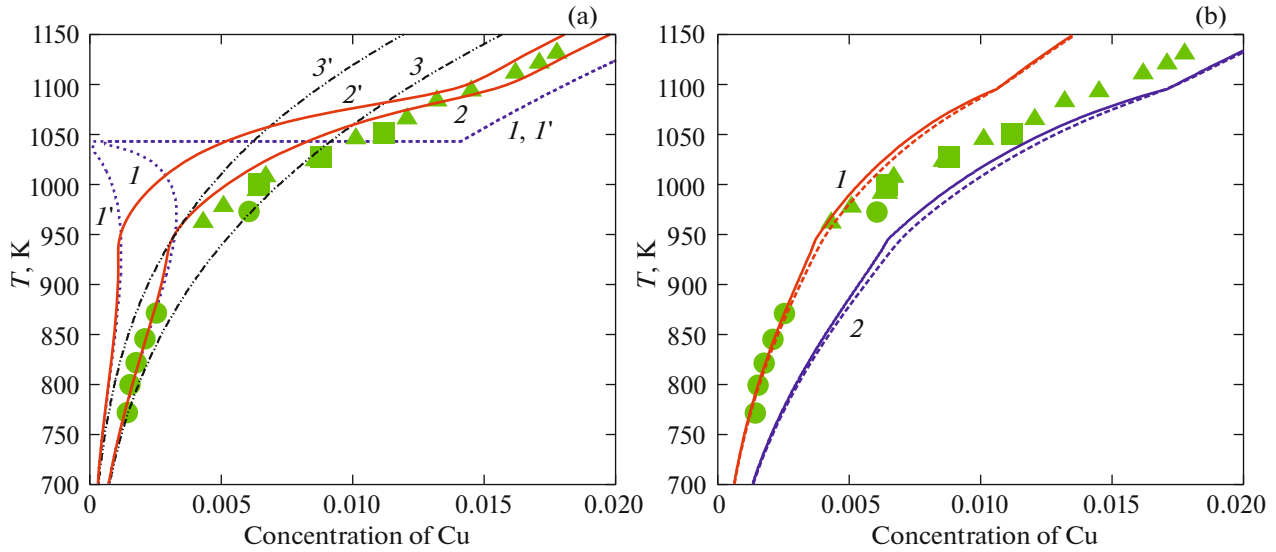


**Fig. 5.** (a) Solubility limit of Cu in a bcc-lattice with a model parameterization via calculating  $J(c)$  by ( $I$ – $3$ ) EMTO-CPA and MCE ( $I'$ – $3'$ ) methods: ( $I$ ,  $I'$ ) only the long-range magnetic order accounted, ( $2$ ,  $2'$ ) the short-range magnetic order (smoothed correlator) accounted, ( $3$ ,  $3'$ ) with a correlator of the spin-lattice dynamics model [27]; (b) solubility limits of ( $I$ ) fcc Cu and ( $2$ ) bcc Fe at choosing  $J_0 = 13.1$  mRy and  $J_1 = 12.7$  mRy; the dotted lines take into account the magnetic entropy. The circles, triangles, and squares are the experimental solubility data for fcc Cu in bcc Fe [6, 29, 30].

Equation (6) describes the free energy in the alloy with a bcc lattice. In the case of a lattice rearrangement of copper precipitates in the bcc structure at high Cu concentrations, Eq. (6) has to be completed with an additional contribution:

$$f_{\text{Fe\_in\_fccCu}}(c) = -\phi + g(c) - TS, \quad (8)$$

where the energy difference between bcc and fcc copper is  $\phi \approx 3.3$  mRy [17].

### 3. THE SOLUBILITY OF BCC AND FCC COPPER AND THE ROLE OF SHORT-RANGE MAGNETIC ORDER

The solubility limit is calculated from the equality of the chemical potential of phases as:

$$\left. \frac{df}{dc} \right|_{c_1} = \left. \frac{df}{dc} \right|_{c_2} = \frac{f(c_2) - f(c_1)}{c_2 - c_1}, \quad (9)$$

where  $c_1$  and  $c_2$  are equilibrium concentrations in phases. The solubility of bcc and fcc copper in the bcc iron matrix is different because Eq. (8). The known experimental data [6, 29, 30] are referred to the solubility of fcc Cu in the bcc Fe matrix. The equilibrium of bcc Cu with a bcc Fe solid solution is metastable by nature; i.e., it takes place at a small size of precipitates (<10 nm) at the beginning of the alloy decomposition. Thus the appropriate solubility limit is unknown from experimental data.

The used mean field approximation allows one to obtain the correct solubility limit at low concentra-

tions ( $\sim 0.02$ ) [20], which is confirmed by the Monte Carlo simulation of the decomposition of the alloy [19]. According to the experiments, the solubility of fcc Cu in bcc Fe is below 0.02 (at  $T = 1150$  K) [6, 29, 30]. With that, it is evident that the solubility limit of bcc Cu is almost 1.5 times higher because the energy difference between bcc and fcc Cu ( $\phi \approx 3.3$  mRy). Thus the solubility of bcc and fcc Cu in the bcc Fe matrix can be accurately described by Eqs. (2)–(9).

Figure 5a displays the calculated solubility of Cu in a bcc matrix, based on the  $J(c)$  dependence obtained via EMTO-CPA (curves  $I$ – $3$ ) and MCE-models (curves  $I'$ – $3'$ ). The experimental data on solubility limit of fcc Cu in bcc Fe were also added as reference. It is seen that the solubility limit evaluated in considering only the long-range magnetic order (curves  $I$  and  $I'$ ) drastically vanishes at  $T = T_C(0) = 1043$  K, which qualitatively contradicts the experiment. The solubility limit plotted with a smoothed correlator taking the short-range magnetic order in account at  $T > T_C$  demonstrates the good agreement with experimental data for the  $J(c)$  dependence calculated via the EMTO-CPA model (curve  $2$ ). Meanwhile, this coincidence is not fully satisfactory, because the theoretical curves describe the solubility of bcc Cu, whereas the experimental results are referred to fcc Cu. The choice of a correlator from the model with a spin–lattice dynamics [27] slightly decreases the qualitative agreement with experiment (curves  $3$  and  $3'$ ). In all cases, choosing the MCE-based  $J(c)$  dependence leads to underestimated solubility limit (curves  $I'$ – $3'$ ).

**Table 1.** Exchange energy parameters at small copper concentrations,  $J(c) = J_0 + J_1c$ 

	EMTO-CPA	MCE	Fitting (Fig. 5b)
$J_0$ , mRy	15.2	13.1	13.1
$J_1$ , mRy	12.7	7.70	12.7

Since the solubility limit is defined by the general tangent rule (9), it remains independent on the  $J(c)$  function at large  $c$ , making thus predominant only coefficients  $J_0$  and  $J_1$  (see Table 1). A decrease in  $J_0$  yields the solubility limit shifted to the right, whereas a decrease in  $J_1$  causes the shift of the solubility limit to the left. Furthermore, the value of  $J_0 = 15.2$  mRy found via the EMTO-CPA calculations seems to be overestimated. Earlier, the independent evaluation of  $J_0 = 14$  mRy was successfully used in the same temperature range in the theory of phase transformation in carbon steel [31]. The best agreement with experiment was found for  $J_0 = 13.1$  mRy (from MCE) and  $J_1 = 12.7$  mRy (from EMTO-CPA). Thus, the solubility limit of fcc Cu is consistent with experiment at  $T < T_C(0)$  (Fig. 5b, curve *I*). However, it deviates to the left from experimental values at high  $T$  temperatures, which can be due to neglected contribution of the entropy nature.

The rough estimation of the role of configuration magnetic entropy  $S_m$  can be performed using the Ising model with a spin of  $1/2$ , for which [23]:

$$S_m = k(1-c) \left\{ \ln 2 - \frac{1}{2} [(1+m) \ln(1+m) + (1-m) \ln(1-m)] \right\}. \quad (10)$$

Meanwhile, the local magnetization in Eq. (10) can be replaced by a spin correlator of  $m \rightarrow \sqrt{Q_1}$  at  $T > T_C$ . The dotted curves in Fig. 5b are plotted taking into account Eq. (10) in the total entropy and exhibit a negligibly small effect. The deviation of the solubility limit from experimental values is likely due to other contributions that remain beyond the consideration, e.g., the vibrational entropy.

#### 4. THE Cu–Cu INTERACTION POTENTIAL AS A FUNCTION OF CONCENTRATION. A PHYSICAL SPINODAL

According to the theory of spinodal decomposition [10, 32], the alloy loses stability relative to infinitely small long-wave composition fluctuations in the convex segment of the  $f(c)$  curve. Therefore the stability limit of the uniform state (spinodal) is determined by the inflection point of the  $f(c)$  curve. The decomposition between a spinodal and a binodal obeys the mechanism of fluctuation nucleation and growth of precipitates. As follows from [33, 34], the classical spinodal

is only a theoretical concept inherent to the mean field approximation and to more accurate methods [20]. The authors of work [35] have assumed that classical spinodal does not look like a physically dedicated line of the phase diagram for real alloy. In connection with this, a schematic phase diagram including the classical nucleation (below the binodal) and spinodal nucleation (above the spinodal) was plotted; the transition between these areas was suggested to be gradual.

Works [36, 37] were dedicated to the discussion of the so-called physical spinodal, or pseudo-spinodal, being the stability limit of a homogeneous alloy relative to heat composition fluctuations (which are not infinitely small). This line was found to exist in either the systems with a long-range potential, or the large molecular weight, such as polymers [38]. As shown in study [19] via the kinetic Monte Carlo (KMC) simulation in a system with a short-range potential (similar to the potential in a FeCu system), the incubation period of homogeneous nucleation tends to the infinity far from the solubility limit and the classical spinodal. The obtained line in a phase diagram is a physical spinodal and expresses the fact that the fluctuation enough for the appearance of critical nucleus is impossible in a homogeneous alloy at a sufficiently low concentration. Thus the physical spinodal limits the homogeneous nucleation area on the phase diagram.

Here we are first to show the KMC calculation of the physical spinodal for a FeCu system with a real concentration-dependent Cu–Cu interaction potential. The local concentration was considered by averaging the occupation numbers over the first coordination sphere around the atoms of each interacting Cu–Cu pair adjacent to nodes of the initial and final positions in jumping. The simulations were implemented for a supercell of  $70 \times 70 \times 70$  unit bcc cells. In order to find a spinodal at each set temperature  $T$ , a series of calculation was conducted at different average concentrations  $c$  for determining a  $c$  value at which the incubation period abruptly changes, so that no decomposition is observed within technically achievable calculation times.

The Cu–Cu interaction potential as a function of concentration can be found from the expansion of the  $g(c)$  function in power of  $c$ :

$$g(c) = K_0 + K_1c + v_{\text{eff}}(c)c^2, \quad (11)$$

where

$$\begin{aligned} K_0 &= -J_0Q_1^0, & Q_1^0 &= Q_1(c=0), \\ K_1 &= (2J_0 - J_1)Q_1^0 = J_0 \left. \frac{dQ_1}{dc} \right|_0, \end{aligned} \quad (12)$$

in accordance with Eq. (2).

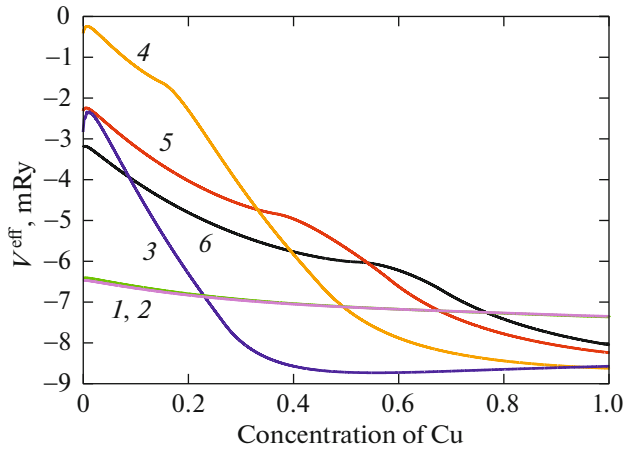


**Fig. 6.** Cu–Cu interaction potentials as a function of Cu concentration, using EMTO-CPA-calculated  $J(c)$ .  $T = 1200$  K (1), 1100 K (2), 1000 K (3), 900 K (4), 800 K (5), 700 K (6).

By virtue of summation over coordination spheres (CSs),  $v_{\text{eff}}(c) = (\sum_p z_p V_p^{\text{eff}}(c))/2$ , the univocal determination of the potential  $V_p^{\text{eff}}(c)$  from Eqs. (11) and (12) is not possible. However, according to work [7], the contribution of the first CS is predominant. Then it is sufficient to consider the nearest neighbors, i.e.,  $z_1 = 8$ ,  $z_p = 0$ , and  $p > 1$ . Thus the concentration-depending Cu–Cu interaction potential is determined from Eqs. (11) and (12) according to the below rule:

$$V^{\text{eff}}(c) = v_{\text{eff}}(c)/4. \quad (13)$$

Note that the PM-state from Eqs. (2) and (11)–(13) results in  $V_{\text{PM}}^{\text{eff}}(c) = v_{\text{PM}}(c)/4$ .

Figure 6 displays the  $V^{\text{eff}}(c)$  potentials calculated from Eqs. (2) and (10)–(12) for various temperatures, using the EMTO-CPA approach for the  $J(c)$  function and the smoothed spin correlator accounting for the short-range order at  $T > T_C$  (curve 3 in Fig. 3, see formulas in Appendix A). As expected from the free energy profile plotted in Fig. 4, the main qualitative feature of  $V^{\text{eff}}(c)$  is an increase in stability of a homogeneous alloy due to the magnetism, i.e., weakening of the potential at low concentrations within a range of intermediate temperatures (immediately above and below the  $T_C$  point of pure iron). At the same time, the potential becomes stronger in the volume of copper precipitates ( $c \sim 1$ ) on account of the effective contribution from the magnetism of a matrix, which is expected to shift the solubility limit (but not the stability limit of a homogeneous state) to the left in comparison with a paramagnetic state.

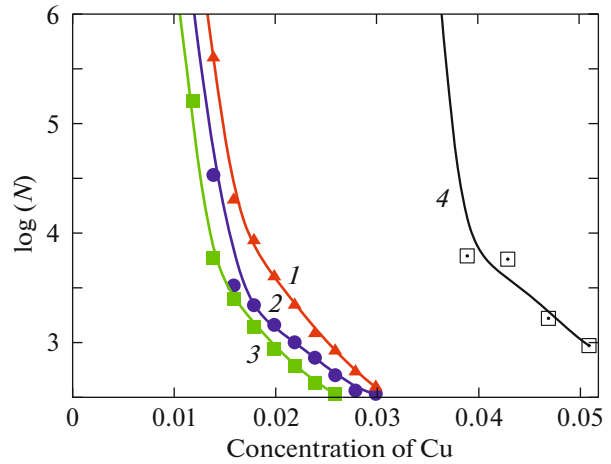


**Fig. 7.** Incubation period of the decomposition in a homogeneous alloy (the sample size is  $70 \times 70 \times 70$  cells) as a function of Cu concentration at  $T = 800$  K (1), 900 K (2), 1000 K (3), 1100 K (4). The calculation is implemented via the KMC method with the potentials given in Fig. 6. The time is expressed by the average number of jumps per Cu atom.

Figure 7 illustrates the incubation periods versus the concentration at various temperatures, calculated using the above potentials. The common qualitative peculiarity is a drastic change in the incubation period with a decrease in  $c$  to a critical value corresponding to the achievement of the physical spinodal.

Figure 8 shows the solubility limit of Cu in the bcc lattice (curve 1) and the physical spinodal (curve 2), both calculated via the Monte Carlo method with potentials given in Fig. 6. The main common feature is a nonmonotonic temperature behavior of the physical spinodal, because of increased stability of the homogeneous alloy relatively small composition fluctuations under the action of the magnetism. On the other hand, a classical spinodal determined by the inflection point in the  $f(c)$  plot was not manifested as a physically dedicated line in the Monte Carlo simulations and is therefore not given here.

Here we discuss the qualitative peculiarities of the model. The quantitative estimation of the position of a physical spinodal may depend on the behavior of the  $J(c)$  exchange energy at the intermediate concentrations, including the coefficients  $J_2$  and  $J_3$  that are different for EMTO-CPA and MCE calculations (see Fig. 1). Meanwhile, since the  $J(c)$  energy is present in Eq. (2) in the form of the  $J(c)Q_1(c)(1-c)^2$  product, where the correlator  $Q_1$  and the multiplier  $(1-c)^2$  vanish at high Cu concentrations, the discrepancy between ab initio EMTO-CPA and MCE simulations (Fig. 1) is expected to make no influence of the qualitative conclusions.

### 5. A KINETIC TTT DIAGRAM. THE EFFECT OF STRUCTURAL DEFECTS ON THE TRANSFORMATION KINETICS

A typical kinetics of decomposition to the right of a physical spinodal in the phase diagram is as follows. The first stage is characterized by the formation of small clusters. The amount of atoms in a solid solution is determined by the Gibbs—Thomson effect rather than by their migration time to the nearest cluster, i.e., by the change in the equilibrium conditions above the surface of small nucleus [39]. Large precipitates grow due to the evaporation of small ones, obeying the Lifshitz—Slezov kinetic law [40]. The larger is the average cluster size the lower is the amount of atoms in a solid solution, approaching the equilibrium solubility limit. As shown in work [41], the growth of precipitates is substantially accelerated at the onset stages due to the vacancy mechanism of diffusion, because vacancies are captured by clusters. Thus the diffusion is implemented by not only singular atoms in a solid solution, but also by the migration of clusters themselves. Although a similar mechanism (collision and merging of droplets as a result of their heat diffusion) was earlier discussed by Binder and Schtauffer [42], it is beyond the consideration in most decomposition models. Since the KMC software used in work [8, 9] implements the direct exchange between the nearest neighbors, the estimation of characteristic times necessitates the introduction of the amendment taking into account the acceleration of the transformation due to the capture of vacancies by clusters.

Curves  $1$  and  $2$  in a phase diagram (Fig. 8) are separated by the area where the decomposition may start only in accordance with a mechanism of heterogeneous nucleation, i.e., after the Cu atoms are segregated at the structural defects (dislocations, grain boundaries, etc.). Curves  $1'$  and  $2'$  in Fig. 8 are referred to the solubility limit (calculated from the remnant concentration in the matrix upon completion of the decomposition) and the stability limit of a homogeneous state at introducing a single dislocation which is simulated via the change in the Cu energy by a value of  $E_{\text{segr}} = -4$  mRy in a tube with a radius equal to a lattice parameter, passing through the center of the cube. It is obvious that the solubility limit remains almost unchanged owing to a small segregation capacitance of a dislocation. At the same time, the stability limit is noticeable shifted to the left, approaching the solubility limit. The transformation kinetics is usually described via the TTT (time—temperature—transformation) diagram that allows one to determine the time necessary for enriching a set degree of decomposition at a defined temperature [7, 43, 44]. The current time at the KMC-simulation is estimated as follows:

$$t = K(T)P\tau, \quad (14)$$

where  $P$  is a number of permutations of the neighboring atoms (per a Cu atom),  $\tau = d^2/D$  is a time for suc-

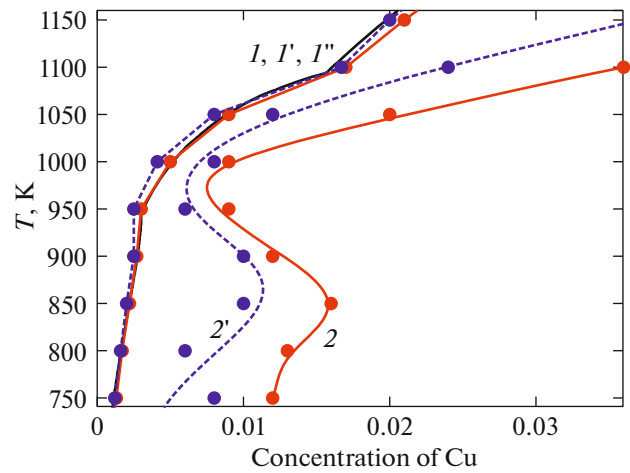


**Fig. 8.** ( $1$ ,  $1'$ ) Solubility and ( $2$ ,  $2'$ ) stability limits of a homogeneous state, evaluated via the KMC method using the potentials given in Fig. 6, in a lack ( $1$ ,  $2$ ) and in the presence ( $1'$ ,  $2'$ ) of a dislocation with a segregation energy  $E_{\text{segr}} = -4$  mRy. The curve  $1'$  is the solubility limit calculated from the chemical potential equality of phases using Eq. (9).

cessful jump of a Cu atom to the neighboring site,  $d = 0.248$  nm is a distance between the nearest nodes in a bcc Fe lattice,  $D$  is a coefficient of diffusion known from the experiment [45, 46], and  $K(T)$  is a correction factor considering some features of the transformation kinetics (accelerated diffusion due to the capture of vacancies by clusters, losses of atoms with time in a solid solution owing to precipitation, accelerated diffusion in the area of dislocations and grain boundaries, change in surface energy of precipitates because the partial violation of the lattice coherence in the interface, sensitivity limit of experimental techniques, etc.).

The analysis reveals (see Appendix B) the relevance to use the  $K(T)$  temperature dependence in the form:

$$K(T) = K_0 \exp[-Q/kT], \quad (15)$$

where  $Q = 55$  mRy in a lack of defects, 102 mRy upon nucleation of precipitates at the dislocations, 141 mRy upon nucleation of precipitates at the grain boundaries (the  $Q$  parameter serves for the approximation of the kinetic curve and it is not an activation energy).

The known experimental data for a TTT diagram [6] are referred to the area between curves  $1$  and  $2$  (see Fig. 8), where, in accordance with our model, the decomposition is possible in only the presence of structural defects. Figure 9 displays the TTT diagram constructed by introducing a single dislocation or a plane grain boundary in a cubic sample (with dimensions of  $80 \times 80 \times 80$  unit cells). The characteristic scale of the defect was chosen to be equal to 2 of a lattice parameter. The degree of decomposition was calculated similarly with that in work [8]). It is seen that

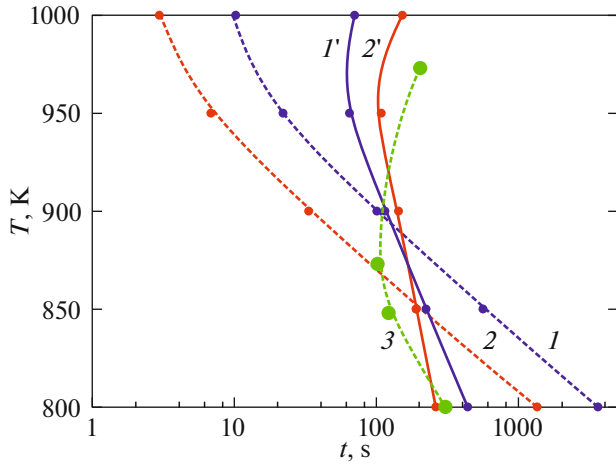


**Fig. 9.** KMC-simulated kinetic TTT diagram. The curves correspond to the degree of decomposition of 10% at simulating the presence of (1, 1') dislocation and (2, 2') grain boundary with a segregation energy  $E_{\text{segr}} = -8$  mRy; (1), (2) without and with (1'), (2') a  $K(T)$  correction coefficient. Curve (3) is referred to experimental data [6].

in the absence of  $K(T)$  the rate of decomposition decreases with decreasing of temperature much faster than in the experiment. On the other hand, the use of  $K(T)$  enables one to achieve the adequate TTT diagram during the nucleation of precipitations at both the dislocation and the grain boundary. Unfortunately, the  $K_0$  coefficient chosen by fitting to experimental data cannot be evaluated (see Appendix B).

Thus, the qualitatively adequate TTT diagram is ensured via the diffusion acceleration and preferable nucleation of precipitations at the defects. The decomposition in the phase diagram area corresponding to experimental data is not implementable in a lack of defects in the present model.

## 6. CONCLUSIONS

The model of decomposition of a FeCu alloy was developed at accounting for the concentration dependence of the magnetic contribution to the free energy. The correct calculation of solubility limit necessitates taking into account the difference between the short-range and long-range magnetic orders in the vicinity of the Curie temperature. The solubility limits calculated for bcc and fcc Cu in a bcc Fe matrix were found to be consistent with experimental values. A concentration-dependent Cu–Cu interaction potential, necessary for the Monte Carlo simulation of the decomposition of alloy, was proposed, as well. The solubility and stability limits of a homogeneous state (physical spinodal) were shown to be different. Furthermore, the physical spinodal exhibits the nonmonotonic temperature dependence. The presence of structural defects, such as dislocations) was found to shift the

stability limit to the left, approaching it to the solubility limit. The influence of structural defects on the kinetic TTT diagram was discussed, as well.

## APPENDIX A

### The Nearest-Neighbor Spin Correlator

A nearest-neighbor spin correlator in considering the long-range magnetic order is determined by the local magnetization  $Q_1(T, c) = m^2(T/T_C, c)$ , where the  $m(T/T_C, c)$  dependence obeys the empirical equation [25]:

$$m(\tau) = [1 - 0.35\tau^{3/2} - 0.65\tau^4]^{1/3}, \quad (\text{A.1})$$

where  $\tau = T/T_C(c)$ .

The short-range order at  $T > T_C$  is taken into account in the qualitative agreement with Oguchi theory

$$Q_1(T) = \begin{cases} m^2(T), & \text{if } T < T^* \\ m^2(T^*) \frac{T^*}{T}, & \text{if } T > T^* \end{cases} \quad (\text{A.2})$$

$$T^* = \beta T_C, \quad \beta = 0.98.$$

The correlator (A.2) exhibits a nonphysical kink at  $T = T^*$ , which is eliminated by smoothing ( $\Delta T = 150$  K)

$$\tilde{Q}_1(T) = \frac{1}{\Delta T} \int_{T-\Delta T/2}^{T+\Delta T/2} Q_1(T') dt'. \quad (\text{A.3})$$

In this case, the magnitude of the short-range magnetic order at  $T > T_C$  is close to that derived in works [47] via the spin-lattice dynamics for a Fe–Ni alloy.

The correlator obtained in the model of spin-lattice dynamics [27] for bcc Fe is also used for comparison. It is approximated by the expression:  $Q_1(T) = 1 - 1/(1 + 0.38\exp[-4.5(T - T_C)/T_C])$  assuming the  $T_C(c)$  dependence for a FeCu alloy.

## APPENDIX B

### The Evaluation of the $K(T)$ Coefficient in the Construction of a TTT Diagram

Represent the  $K(T)$  function as a product  $K(T) = K_0 K_V(T) K_{SS}(T) K_{\text{def}}(T)$ .

A multiplier  $K_V(T)$  accounts for the diffusion acceleration due to the capture of vacancies by clusters. If the diffusion is carried out by clusters of two atoms (which can be valid at the decomposition onset), then  $K_V(T) \sim \exp[-Q_V/kT]/3$ ,  $Q_V = 25.7$  mRy [16].

A multiplier  $K_{SS}(T)$  describes the fraction of Cu atoms in a solid solution, which varies with time and approaches the equilibrium solubility limit at attaining the local equilibrium, then  $K_{SS}(T) \sim \exp[-v/kT]/c_0$ , where  $v \sim 28.8$  mRy.

**Table 2.** Diffusion coefficient ratio of Cu in the bulk, on the dislocation and at the grain boundary of a bcc-Fe matrix in accordance with data [45, 46, 48, 49]

$\frac{D_{\text{bulk}}^{1000\text{ K}}}{D_{\text{bulk}}^{800\text{ K}}} \text{ (Cu in Fe)}$	$\frac{D_{\text{disl}}^{1000\text{ K}}}{D_{\text{disl}}^{800\text{ K}}} \text{ (Cu in Cu)}$	$\frac{D_{\text{GB}}^{1000\text{ K}}}{D_{\text{GB}}^{800\text{ K}}} \text{ (Cu in Fe)}$
567	85	18

A multiplier  $K_{\text{def}}(T)$  accounts for the diffusion acceleration on defects. Based on the fact that the rate of diffusion behaves as  $\sim \exp[-Q/kT]$ , as well as using the known coefficients of diffusion of Cu in the bulk, on the dislocation and at the grain boundary in a bcc Fe matrix (see Table 2), one obtains  $K_{\text{def}}(T) \sim \exp[-Q_{\text{def}}/kT]$ , where  $Q_{\text{def}} = 47$  mRy for a dislocation and 86 mRy for a grain boundary. The use of  $K_{\text{def}}(T)$  parameter implies that nucleation and growth of precipitations are controlled by the diffusion on the appropriate defects.

The temperature-independent  $K_0$  coefficient in the construction of a TTT diagram was chosen by fitting to experimental data. Among the neglected factors, one can mention the real density of the number of defects (calculations involve a single dislocation or a grain boundary) and the variation in the surface energy of precipitations because the partial violation of the lattice coherence at the interface.

#### ACKNOWLEDGMENTS

The authors are sincerely grateful to Professor Yu.N. Gornostyrev for useful discussions.

#### FUNDING

This work was supported within the framework of a State Task on the “Magnit” (project AAAA-A18-118020290129-5) and “Struktura” (project AAAA-A18-118020190116-6) Topics.

#### REFERENCES

- W. C. Leslie and E. Hornbogen, in *Physical Metallurgy*, Ed. by R. W. Cahn and P. Haasen (North-Holland, Amsterdam, 1996).
- S. Vaynman, R. S. Guico, M. E. Fine, and S. J. Manganello, *Met. Trans. A* **28**, 1274 (1997).
- A. Deschamps, M. Militzer, and W. J. Poole, *ISIJ Int.* **41**, 196 (2001).
- P. J. Othen, M. L. Jenkins, and G. D. W. Smith, *Philos. Mag. Lett.* **70**, 1 (1994).
- G. R. Odette and G. E. Lucas, *Rad. Effect Defects Solids* **144**, 189 (1998).
- M. Perez, F. Perrard, V. Massardier, X. Kleber, A. Deschamps, H. de Monestrol, P. Pareige, and G. Covarel, *Philos. Mag.* **85**, 2197 (2005).
- O. I. Gorbatov, I. K. Razumov, Yu. N. Gornostyrev, V. I. Razumovskiy, P. A. Korzhavyi, and A. V. Ruban, *Phys. Rev. B* **88**, 174113 (2013).
- I. G. Shmakov, I. K. Razumov, O. I. Gorbatov, Yu. N. Gornostyrev, and P. A. Korzhavyi, *JETP Lett.* **103**, 112 (2016).
- I. K. Razumov, *JETP Lett.* **107**, 369 (2018).
- J. Christian, *Theory of Transformations in Metals and Alloys* (Pergamon, Oxford, 1975; Mir, Moscow, 1978).
- H. Harvig, G. Kirchner, and M. Hillert, *Met. Trans.* **3**, 329 (1972).
- L. H. Chen, T. S. Chin, and M. Hung, *J. Appl. Phys.* **64**, 5962 (1988).
- T. Nishizawa, M. Hasebe, and M. Ko, *Acta Metall.* **27**, 817 (1979).
- C. Zener, *Trans. AIME* **167**, 550 (1946).
- C. Zener, *Trans. AIME* **203**, 619 (1955).
- F. Soisson and C.-C. Fu, *Phys. Rev. B* **76**, 214102 (2007).
- V. N. Urtsev, D. A. Mirzaev, I. L. Yakovleva, N. A. Tereshchenko, and K. Yu. Okishev, *Phys. Met. Metallogr.* **110**, 346 (2010).
- D. Reith, M. Stöhr, R. Podloucky, T. C. Kerscher, and S. Müller, *Phys. Rev. B* **86**, 020201 (2012).
- I. K. Razumov, *Phys. Solid State* **59**, 639 (2017).
- K. Yu. Khromov, F. Soisson, A. Yu. Stroevev, and V. G. Vaks, *J. Exp. Theor. Phys.* **112**, 414 (2011).
- Y. Wang, H. Hou, J. Yin, S. Hu, X. Liu, F. Xue, C. H. Henager, Jr., and J. Wang, *Comput. Mater. Sci.* **145**, 163 (2018).
- J.-F. Gouyet, M. Plapp, W. Dieterich, and P. Maas, *Adv. Phys.* **52**, 523 (2003).
- J. Ziman, *Models of Disorder: The Theoretical Physics of Homogeneously Disordered Systems* (Cambridge Univ., Cambridge, New York, 1979; Mir, Moscow, 1982).
- K. Sumiyama, T. Yoshitake, and Y. Nakamura, *J. Phys. Soc. Jpn.* **53**, 3160 (1984).
- M. D. Kuz'min, *Phys. Rev. Lett.* **94**, 107204 (2005).
- J. S. Smart, *Effective Field Theories of Magnetism* (Saunders, London, 1966; Mir, Moscow, 1968).
- P.-W. Ma, C. H. Woo, and S. L. Dudarev, *Phys. Rev. B* **78**, 024434 (2008).
- D. Isheim, M. S. Gagliano, M. E. Fine, and D. N. Seidman, *Acta Mater.* **54**, 841 (2006).
- G. Salje and M. Feller-Knipmeier, *J. Appl. Phys.* **48**, 1833 (1977).
- G. R. Speich, J. A. Gula, and R. M. Fisher, in *Electron Microprobe*, Ed. by T. D. McKinley, K. J. Heinrich, and D. B. Witty (Wiley, New York, 1966).
- I. K. Razumov, D. V. Boukhvalov, M. V. Petrik, V. N. Urtsev, A. V. Shmakov, M. I. Katsnelson, and Yu. N. Gornostyrev, *Phys. Rev. B* **90**, 094101 (2014).
- A. G. Khachatryan, *Theory of Phase Transformations and the Structure of Solid Solutions* (Nauka, Moscow, 1974) [in Russian].
- Z.-G. Wang, *J. Chem. Phys.* **117**, 481 (2002).
- G. Wilemski and J.-S. Li, *J. Chem. Phys.* **121**, 7821 (2004).
- K. Binder, *Phys. Rev. A* **29**, 341 (1984).

36. A. Z. Patashinskii and B. I. Shumilo, *Sov. Phys. Solid State* **22**, 655 (1980).
37. S. M. Wood and Z. G. Wang, *J. Chem. Phys.* **116**, 2289 (2002).
38. A. A. Lefebvre, J. H. Lee, N. P. Balsara, and B. Hammouda, *J. Chem. Phys.* **116**, 4777 (2002).
39. D. Perez and L. Lewis, *Phys. Rev. E* **74**, 031609 (2006).
40. I. M. Lifshits and V. V. Slyozov, *J. Phys. Chem. Solids* **19**, 35 (1961).
41. F. Soisson and C. C. Fu, *Phys. Rev. B* **76**, 214102 (2007).
42. K. Binder and D. Stauffer, *Adv. Phys.* **25**, 343 (1976).
43. G. Stechauner and E. Kozeschnik, *Adv. Mater. Res.* **922**, 728 (2014).
44. G. Stechauner and E. Kozeschnik, *Acta Mater.* **100**, 135 (2015).
45. B. Jönsson, *Z. Metallkd.* **83**, 349 (1992).
46. Y. Liu, L. Zhang, Y. Du, and D. Liang, *CALPHAD* **33**, 732 (2009).
47. A. K. Zhuravlev and Yu. N. Gornostyrev, *J. Exp. Theor. Phys.* **119**, 503 (2014).
48. D. B. Butrymowicz, J. R. Manning, and M. E. Read, *J. Phys. Chem. Ref. Data* **2**, 643 (1973).
49. *Diffusion in Solids Metals and Alloys. Landolt-Börnstein New Series* (Springer, Berlin, 1990), Vol. III/26.

*Translated by O. Maslova*